Acta Geotechnica (2023) 18:757–775
https://doi.org/10.1007/s11440-022-01607-4

RESEARCH PAPER

Characterization of hydraulic fracture configuration based on complex in situ stress field of a tight oil reservoir in Junggar Basin, Northwest China

Can Shi[1,2] · Botao Lin[1,3] · Huiyong Yu[4] · Shanzhi Shi[4] · Jiahao Zhang[1]

Received: 28 October 2021 / Accepted: 14 May 2022 / Published online: 28 June 2022

Abstract

The Jurassic Badaowan formation of the tight oil reservoir in northwest Xinjiang, China, is featured by a complex in situ stress pattern, leading to an unclear understanding of the orientation and geometry of a propagated hydraulic fracture. In this regard, a three-dimensional (3-D) in situ stress field was first configured based on a detailed mechanical earth model of the region of concern. Secondly, a fluid-solid-damage coupling model was established to explore the influences of the in situ stresses and the engineering parameters on fracture propagation. Finally, a systematic approach was proposed to characterize the updated stress field and the fracture morphology reconfigured by the in situ stress. The findings disclose that the reservoir is mainly controlled by reverse faults that generate horizontal fractures in most parts of the region. The in situ stress follows the strike-slip fault pattern where vertical fractures are dominant in the central and southeastern part of the reservoir, where the vertical fracture tends to be constrained in the oil layer when the interlayer minimum stress difference ΔS_{h} becomes greater than 4 MPa in the southeast. In addition, as the injection rate increases, the width of a fracture increases, whereas its height decreases. The viscosity has negligible effect on the fracture height, but its increase can enlarge the fracture width and decrease the length. Here, the cross-dipole shear wave logging record in a field well was used to verify the proposed method, showing that the predicted fracture morphology was consistent with the field test result. The research can aid field engineers in predicting fracture morphology for optimizing a fracturing scheme.

Keywords Cohesive zone method · Hydraulic fracture · In situ stress · Interlayer stress difference · Tight oil reservoir

1 Introduction

It is widely recognized that unconventional oil and gas reservoirs have become major hydrocarbon plays in recent years. The Jurassic Badaowan formation in Xinjiang province, northwest China, has one of the largest tight oil reservoirs in the world. The associated reservoirs are radical burial depth variation, extremely low porosity, poor permeability, and substantial heterogeneity. Therefore, hydraulic fracturing has become a necessary and routine stimulation method in the developed region. The tectonic activities in the geological history of this region produced complex in situ stress fields, making it difficult to determine the orientation of the hydraulic fracture planes. It was discovered that some hydraulic fractures propagate vertically, whereas others expand along the horizontal plane. A good example of vertical fractures occurred in a formation with a high water-bearing layer beneath it. After fracturing, the water cut of the well increased dramatically, implying that the HFs had communicated with the water layer.

On the other hand, the microseismic monitoring results of Wells tagged T006-T008 confirmed that the hydraulic fractures at the formation depth developed horizontally and symmetrically in two wings. Fracture morphologies largely

✉ Botao Lin
linbotao@vip.163.com

1 College of Petroleum Engineering, China University of Petroleum, Beijing 102249, China

2 Department of Civil and Environmental Engineering, University of Alberta, Edmonton, AB, Canada

3 College of Artificial Intelligence, China University of Petroleum, Beijing 102249, China

4 Xinjiang Oilfield Company, Engineering Technology Research Institute, Karamay, China

determine the stimulated reservoir volume and the transport of proppants, henceforth affecting the production. When hydraulic fractures develop horizontally (Fig. 1a) or vertically but without penetration to the interlayers (Fig. 1b), the fractures are restricted to propagate within the oil, for which perforation and fracturing are required. On the other hand, if the vertical fractures can penetrate the interlayer, only the oil layer needs to be perforated and fractured (Fig. 1c). In addition, if there exists a high water-bearing layer beneath the oil layer, the vertical fractures may communicate with the water layer, resulting in a decline in productivity. Therefore, the vertical fracture propagation behavior affects the fracturing design and the oil production.

Many researchers have pointed out the importance of the in situ stress field and its influences on fracture paths. A commonly recognized phenomenon is that a hydraulic fracture forms perpendicular to the least principal stress [1, 2]. Therefore, the key in determining the directions of hydraulic fractures relies heavily on a detailed characterization of the in situ stress. In this regard, various geomechanical models were constructed to evaluate the formation's in situ stress and rock mechanical parameters before hydraulic fracturing simulation [3, 4]. The common parameters assessed are rock mechanical properties and in situ stress from analyzing the logging data, including Young's modulus (E), Poisson's ratio (μ) [5–10], and the maximum and minimum principal horizontal stresses (S_{H} and S_{h}) [11–14].

In addition, the field measurements show that the horizontal stresses are highly dependent on stratigraphical lithology. For example, some tight formations are distributed with lots of low-permeability mudstone interlayers, which lead to larger minimum horizontal stresses than the neighboring layers [15–18]. Therefore, a strong variation of stratigraphical lithology can lead to significant contrast in horizontal stress magnitudes among different layers, and further affects the extension of vertical hydraulic fractures [19, 20]. It hasS been discovered that the difference in minimum horizontal stress ΔS_{h} plays a key role in influencing vertical fracture propagation [21, 22]. Warpinski et al. [23] argued that a magnitude of ΔS_{h} at 2–3 MPa is adequate to restrain the vertical extension of hydraulic fractures for Tennessee and Nugget sandstone, which was verified from the field results [25, 26]. Teufel et al. [24] and Jin et al. [27] conducted true-triaxial hydraulic fracturing tests on the Arizona, Berea, Coconino, and Tennessee sandstones and came to similar conclusions.

The permeability of the formation and the viscosity of the injected fluid can also affect the vertical propagation of a hydraulic fracture [28]. The simulation of hydraulic fracturing has been conducted using a variety of numerical methods, including boundary element method (BEM) [29, 30], the discrete element method (DEM) [32, 33], the extended finite element method (XFEM) [31], and the cohesive zone finite element method (CZM). The BEM method requires re-meshing during fracture propagation, while the DEM method has limitations in handling large-scale fracture propagation problems due to computational efficiency. Meanwhile, the XFEM method has many difficulties computing three-dimensional fracture propagation at the current stage. The CZM method is an effective approach for quantitative analysis of fracture behavior through explicit simulation of the fracture processes, which can simulate the initiation and propagation of a fracture and the evolution of bottomhole pressure [34–37]. The CZM assumes a predefined planar cohesive layer on which the fractures propagate and therefore restricts the direction of fracture propagation. Compared to other simulation methods, the CZM is capable of modeling damage evolution inherent in hydraulic fracture development at a borehole [38]. It can also avoid the singularity at the crack tip region and fit naturally into the conventional finite element

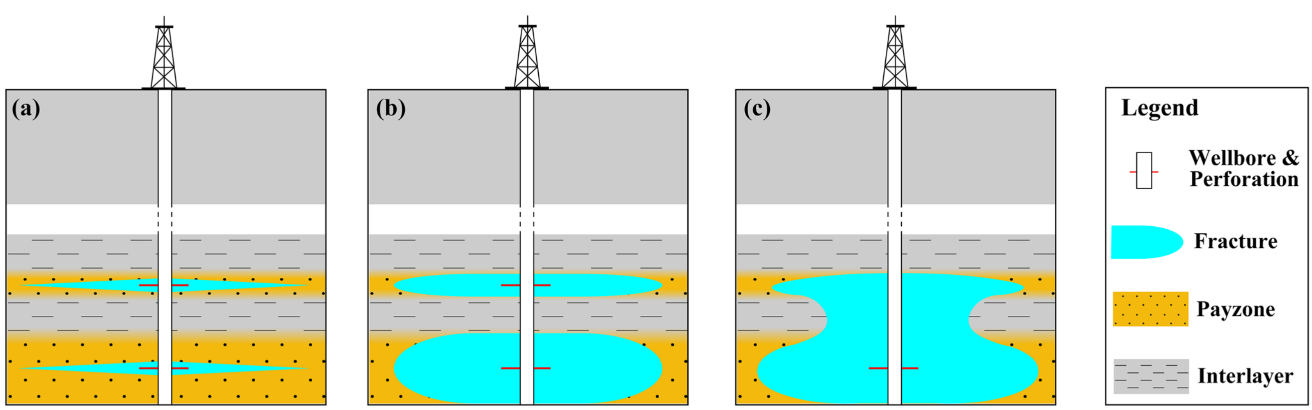

Fig. 1 Impact of fracture propagation on fracturing design

method [36, 39]. In this regard, 3-D CZM has incomparable advantages in investigating the propagation of fractures and predicted the height, length, and aperture of a hydraulic fracture [22, 37]. The above studies show that three-dimensional CZM is suitable for the study of fracture propagation morphology. In addition, this paper mainly studies the longitudinal expansion of hydraulic fractures, focusing on the fracture propagation in the plane perpendicular to the horizontal minimum stress, so CZM was chosen to be used for analysis.

To the best of authors' knowledge, little research has been conducted to describe the in situ stress distribution and the associated fracture propagation in tight oil formations scattered with interlayers. Therefore, a case study in the Jurassic Badaowan Formation is conducted to investigate the fracture propagation in a complex in situ stress field. To achieve this goal, a three-dimensional in situ stress field for the Badaowan formation in the No.7 region, Junggar Basin was built based on available geological data. Then, the cohesive zone method was applied to evaluate the influences of in situ stresses and engineering parameters on the fracture propagation, providing the detailed characterization of the geophysical and geomechanical properties of the studied formation.

2 Geology and geomechanical properties

2.1 Geological and geomechanical characteristics

The Badaowan formation in the No.7 region is located at the Junggar Basin, east of Karamay city at north Xinjiang province, northwest China. The plan view of the research region of the No.7 region Badaowan formation is displayed in Fig. 2. The Badaowan formation of the No.7 region has a monoclinic structure that inclines from the northwest towards the southeast. The inclination of the strata in the central and northern region is gently dipped at an angle of 6–15°. The angle gradually increases towards the southeast up to 30°. The depth of the formation ranges from 640 to 1500 m, covering a thickness between 51 and 251 m that is averaged at 108 m. Two large-scale reverse faults are bordering the region: the Karamay-Urho fault and the south Baijiantan fault. Also, three minor faults exist inside the region, numbered 5054, 5057, and 5137.

The sedimentary facies of the formation are outlined in Well T002 as an example in Fig. 3. As illustrated in Fig. 3, the Badaowan Formation overlies the Jurassic Sangonghe Formation and is underlaid by Triassic Baijiantan Formation. The mineralogy of the Badaowan formation is mainly composed of conglomerate, mudstone, and sandstone. The lithology ranges from conglomerate to fine sandstone from bottom to top, along which the particle size varies from coarse to fine. The oil layer is dominated by sandstone and conglomerate, where the sandstone part provides most of the resources. The lithology variation leads to strong heterogeneity of the physical and mechanical properties. Mudstone widely distributes across the formation and has the lowest permeability and porosity. The diagenetic conglomerate layers are featured by argillaceous cementation, demonstrating much lower porosity and permeability but a larger Poisson's ratio than the sandstone layers. The lithological pattern in the studied formation leads to a complex distribution of in situ stresses field in the region of concern.

A series of triaxial compression tests and permeability experiments were conducted on 25 mm × 50 mm cylindrical core samples collected from wells T001-T003. The measured geomechanical properties, including porosity, permeability, Young's modulus, and Poisson's ratio are listed in Table 1.

2.2 In situ-stress characterization

The extended leak-off test (XLOT) was carried out on well T004 and analyzed using the modified G-function method. The G-function was first proposed by Nolte et al. [41, 42] to describe the decline of fracture pressure during leak-off test. Barree and Mukherjee [43] presented a G-function derivative method for analyzing the fracture injection tests. The leak-off type and the fracture closure pressure (FCP) can be identified according to the derivative of pressure (dP/dG) and the "superposition" derivative (GdP/dG) versus the G-function curves. In a G-function derivative analysis, the normal leak-off occurs when the GdP/dG curve lies on a straight line through the origin. The fracture closure pressure can subsequently be determined at the moment when the GdP/dG curve deviates downward from the straight line [44]. The fracture closure pressure (FCP) was automatically detected from the point of deviation from the initial straight line [45], being equal to the minimum horizontal stress (Fig. 4). If the flow rate and fluid viscosity are low enough, the fracture propagation pressure (FPP) is close to the least principal stress [46]. However, if a viscous frac fluid is used, or a frac fluid with suspended proppant, FPP will increase due to large friction losses. In such cases, the fracture closure pressure (FCP) is a better measure of the least principal stress than the FPP [3]. The viscosity of the fracturing fluid in Well 004 is 30 mPa·s and contains proppant. In this case, FCP is more suitable as the minimum principal stress. In addition, the Kaiser acoustic emission tests were carried out on core samples of different depths in Well T002.

Locating stress orientation is crucial in solving wellbore stability and hydraulic fracturing problems. The in situ

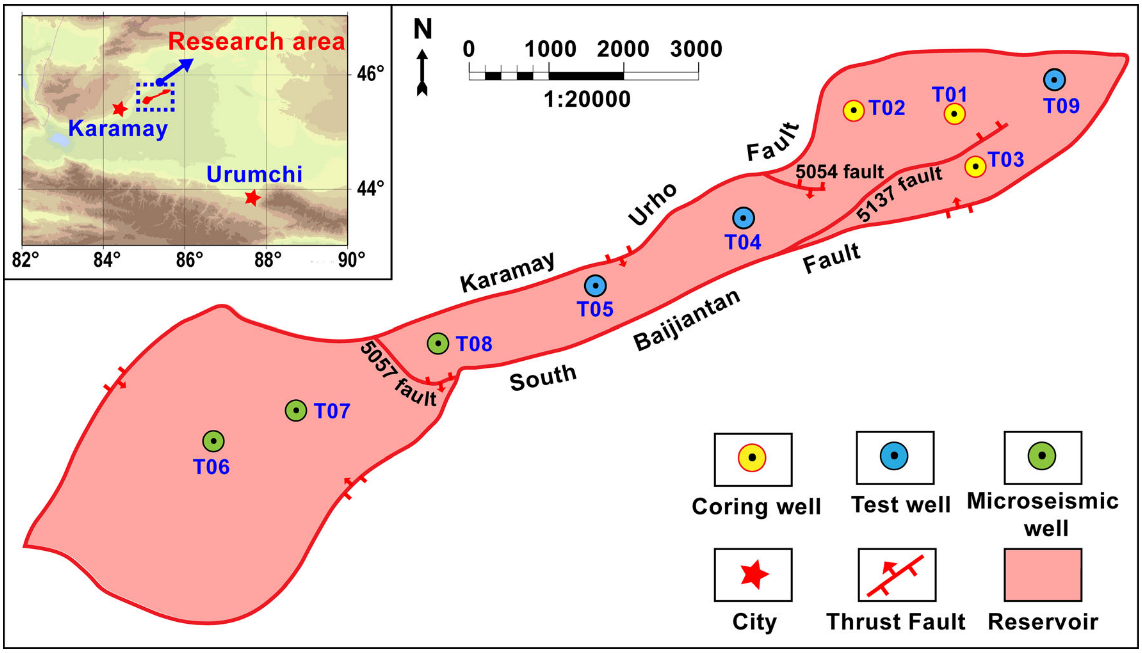

Fig. 2 Location of the region of concern and distribution of faults

stress orientation is commonly determined from the recorded borehole features, such as breakout configuration interpreted from caliper data, Formation Micro-Imager logs (FMI), and microseismic events. When part of the wellbore collapses in a vertical well, it develops an elliptical cross section with the long axis of the ellipse aligned parallel to S_h [47]. In addition, given that hydraulic fractures propagate in the direction of S_H, either the FMI or the microseismic records can be used to determine the stress direction [3]. This study analyzed the six-arms caliper data of Well T002 to derive the stress azimuth. The ellipse method was used to construct the cross-sectional shape of Well T002, which provides the true center of the wellbore for both elliptical and circular borehole shapes [48]. It was disclosed that a borehole collapse occurs at a depth of 720 m, producing the S_H azimuth to be NE81° (Fig. 5a). Besides, the S_H azimuth was also obtained at a depth of 1170–1249 m from estimating the plane that contains most of the recorded microseismic events (Fig. 5b and c).

The magnitude and orientation of the measured in situ stresses are summarized in Table 2. as attained from the field or laboratory tests represent specific depths in wells evenly spread over the region of interest. They are used as benchmarks for a detailed characterization of in situ stresses of the formation that are achieved via the interpretation of logging data from 213 wells in the region.

3 Establishment of the mechanical earth model and the fracture model

3.1 Overall procedure

The Badaowan Formation in the No.7 region was selected as the object of concern. The procedure can be divided into (1) establishment of a mechanical earth model for describing the formation; (2) formulating a hydraulic fracture model to simulate its propagation based on the former geomechanical model. The mechanical earth model was constructed to describe the in situ stresses and rock mechanical parameters of the formation, including the three principal stresses (S_v, S_H, and S_h), the pore pressure (P_p), and the rock mechanics properties. The rock mechanics properties comprise the unconfined compressive strength (UCS), tensile strength (T_0), internal friction angle (ϕ), Young's modulus (E), and Poisson's ratio (μ). Figure 6 shows the used geomechanical data for constructing the geomechanical models.

The mechanical earth model was built as follows. First, lithological classification was implemented based on the downhole core and logging data. Secondly, the relationship between the dynamic and the static mechanical parameters was obtained to convert the former as collected from the logging data to the latter. Finally, the magnitude and orientation of the in situ stress were analyzed from both field tests and laboratory experiments, based on which a 3D in situ stress field was constructed using the Kriging

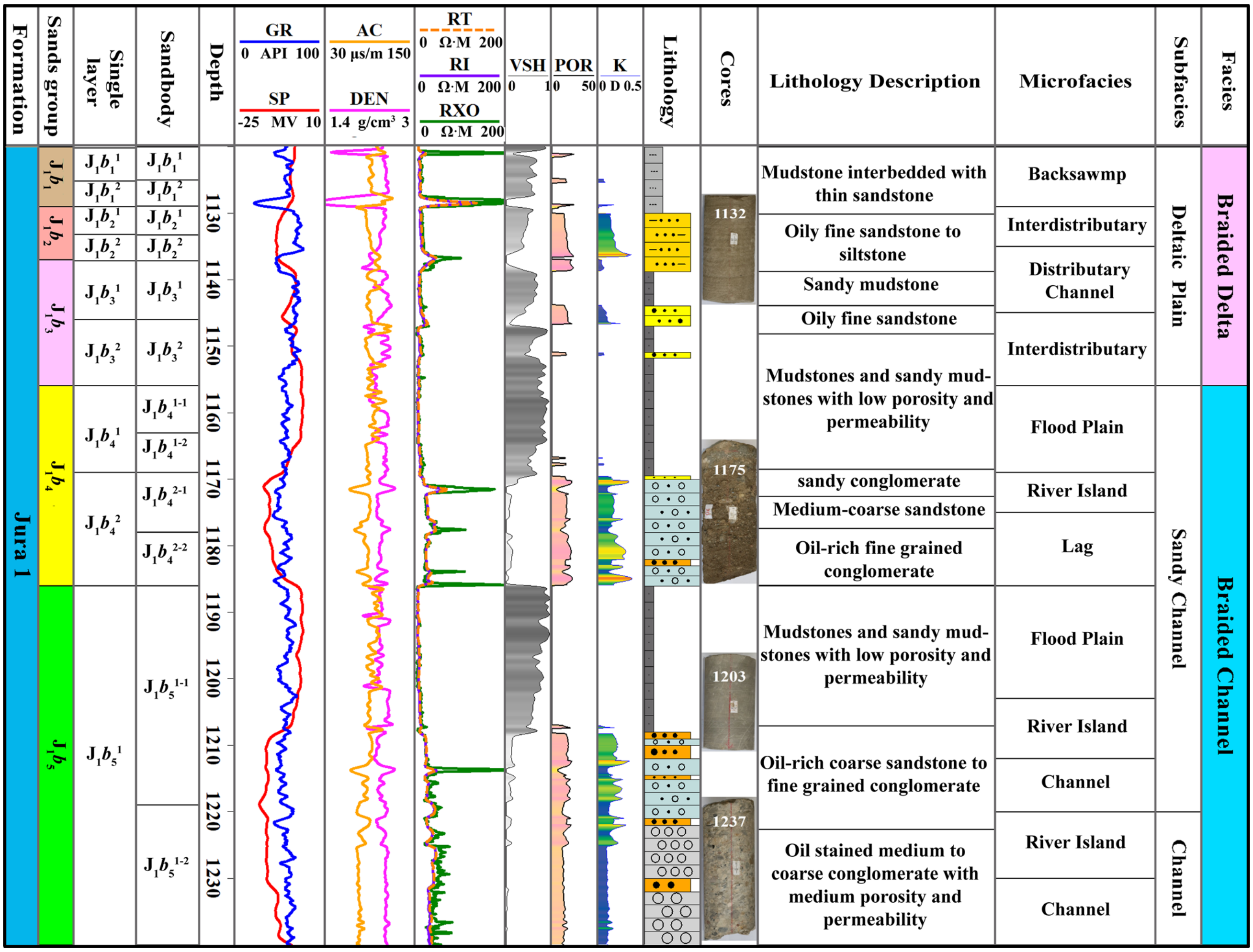

Fig.3 Sedimentary facies at well T002 in the region

Table 1 Geomechanical properties of the studied formation layers

Layer	Depth (m)	Lithology (–)	Porosity (%)	K_v (mD)	K_h (mD)	E (GPa)	μ (–)	UCS (GPa)	S_t (GPa)
$J_1b_1^1$	1123	Mudstone	3.4	8.1	12.5	18.5	0.24	70.41	6.18
$J_1b_2^2$	1132	Sandstone	16.2	282.3	310.2	13.1	0.20	66.43	5.87
$J_1b_3^1$	1146		12.3	163.6	203.4	12.7	0.21	64.94	5.09
$J_1b_4^2$	1175	Conglomerate	20.5	258.7	364.2	19	0.27	68.65	6.10
	1182		19.3	203.2	230.1	15.3	0.26	71.47	5.63
$J_1b_5^1$	1196		18.1	231.8	227.3	21	0.24	71.5	6.32
	1237		17.2	141.7	148.3	23	0.25	92.25	7.77

interpolation method. Given the mechanical earth model that combines the geomechanical properties and the in situ stress field, a customized cohesive zone method was used to study the influence of the interlayer stress difference ΔS_h, fluid viscosity, and injection rate on the hydraulic fracture propagation. The complete technical procedure taken in this study is shown in Fig. 7.

3.2 Calculation of the rock mechanics properties and in situ stresses

The mechanical properties of the rock control the mechanical response of rocks to changes in in situ stresses. The rock mechanics properties such as Young's modulus (E), Poisson's ratio (μ), uniaxial compressive strength (UCS), tensile strength (S_t), internal friction angle (ϕ), and

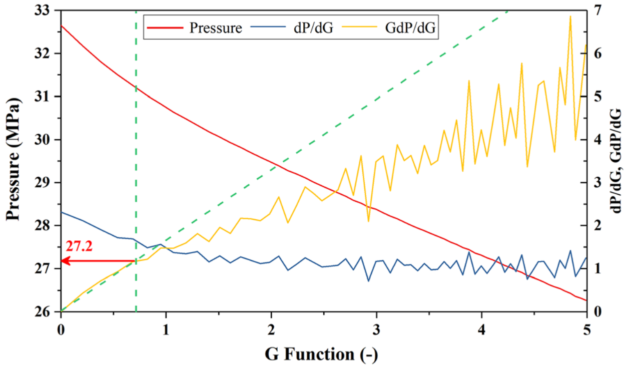

Fig.4 G function method to analyze the XLOT test result

cohesion (S_0) form key parts of the geomechanical model. The dynamic elastic modulus and Poisson's ratio can be obtained by using the longitudinal and shear wave velocity [5]

$$E_d = \frac{\rho v_s^2 [3(v_p/v_s)^2 - 4]}{(v_p/v_s)^2 - 1} \quad (1)$$

$$\mu_d = \frac{(v_p/v_s)^2 - 2}{2[(v_p/v_s)^2 - 1]} \quad (2)$$

where E_d is the dynamic Young's modulus (MPa), μ_d is the dynamic Poisson's ratio (dimensionless), v_p is the longitudinal wave ($m/\mu s$), v_s is the shear wave ($m/\mu s$), and ρ is the density (kg/L).

It must be noted that the dynamic rock elastic parameters obtained by the acoustic logging data reflect the mechanical properties of the formation when it is instantaneously loaded, which is different from the long static load experienced by the formation. The ratio between dynamic and static moduli was found to range between 1 and 20 [49]. Lower ratios usually occur in stiff rocks, while higher ratios are often found in relatively soft sediments. Moreover, the parameters used for the conversion also depend on lithology [50]. Therefore, it is necessary to clarify the lithology profile of the formation. In this

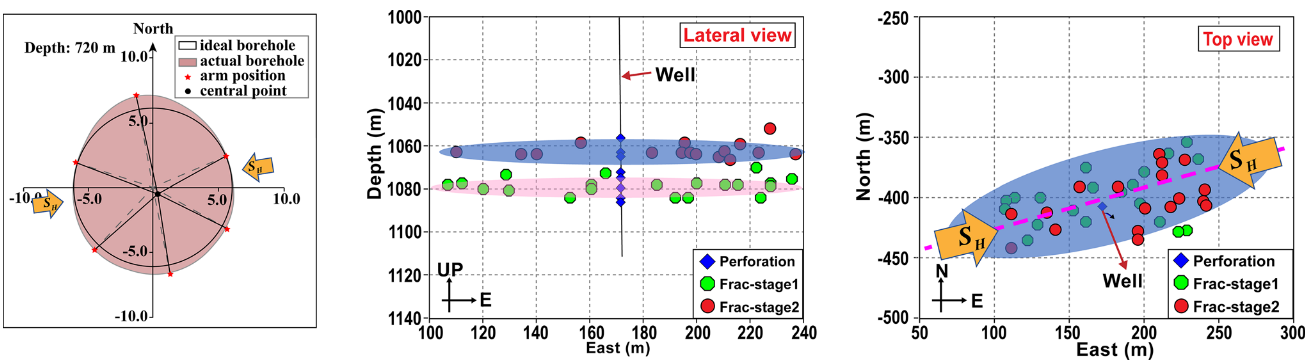

Fig.5 Determination of the direction of S_H in well T002: (a) wellbore shape described by six-arms caliper; (b) side view of the microseismic events; (c) plan view of the microseismic events

Table 2 Summary of in situ stress characteristics

Stress	Method	Layer	Well	Depth (m)	Results
Magnitude S_H/ S_h/ S_v (GPa)	Kaiser test	$J_1b_1^1$	T002	1123	28.5/27.2/25.6
		$J_1b_2^2$		1132	28.7/26.4/25.3
		$J_1b_3^1$		1146	28.1/27.2/25.9
		$J_1b_4^2$		1175	29.2/27.9/26.2
		$J_1b_5^1$		1237	32.2/29.8/28.7
	XLOT	$J_1b_5^1$	T004	1229	Sv-27.2
Orientation	6-arms Caliper	$J_1b_4^2$	T005	720	NE81 °
	Microseismic	$J_1b_4^2$	T006	1170–1184	NE77 °
		$J_1b_5^1$	T007	1240–1249	NE82 °
		$J_1b_5^1$	T008	1234–1246	NE88 °
Average					NE82 °

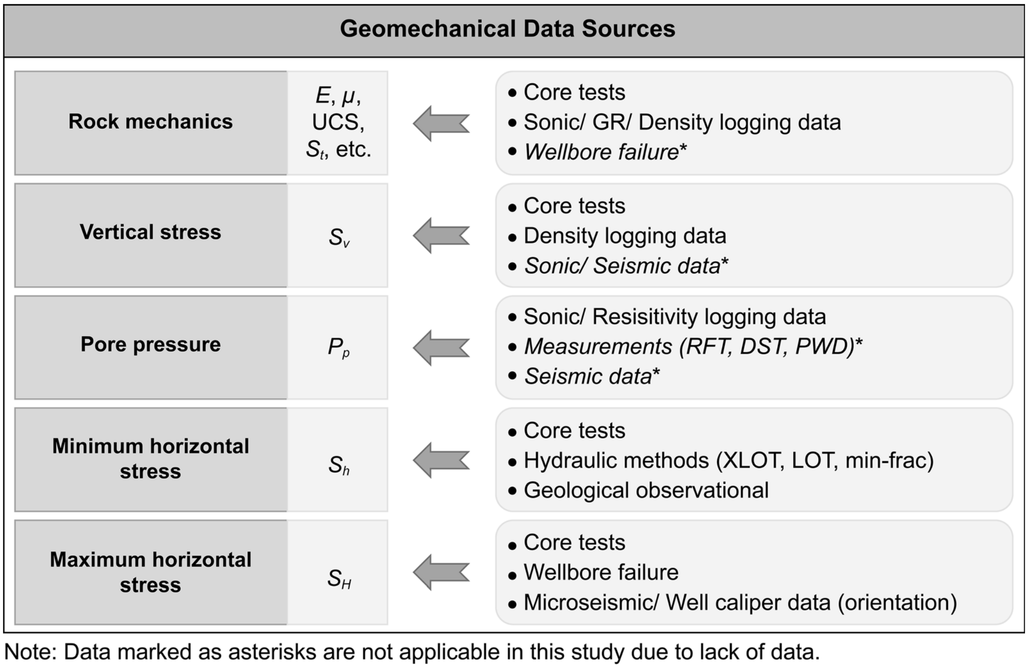

Fig.6 Parameters used to construct the mechanical earth model and the derivation methods

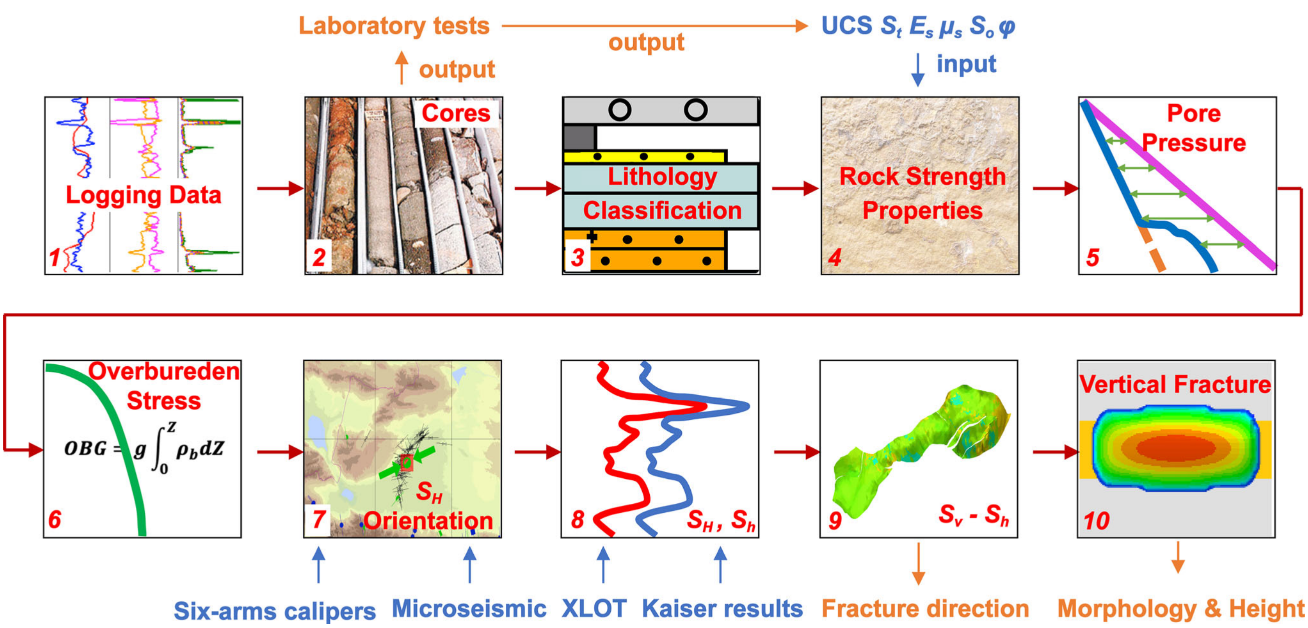

Fig.7 Flow chart of the technical procedure

research, the on-site cores were used to classify the lithology of the studied area [51]. First, the lithological information of the downhole cores of well 1 to well 3 was collected with the logging data at the corresponding core depths to generate data points that combine information including rock type, CNL (compensated neutron logging), RT (true formation resistivity), DEN (density logging), AC (acoustic logging), and GR (natural gamma-ray logging). Secondly, the data points are cross-plotted at different colors that distinguish the lithologies (Fig. 8). Finally, the classification criteria of lithology were derived from the cross-plots. Figure 8 shows that only the CNL-RT cross-plot can develop clear boundaries for different lithologies, while others have a strong overlap of the data points that represent different lithologies. Therefore, the lithology classification criteria of the study area are determined from the blue dashed line in Fig. 8a: the rock type is mudstone when RT is below 11, sandstone if CNL is greater than 26,

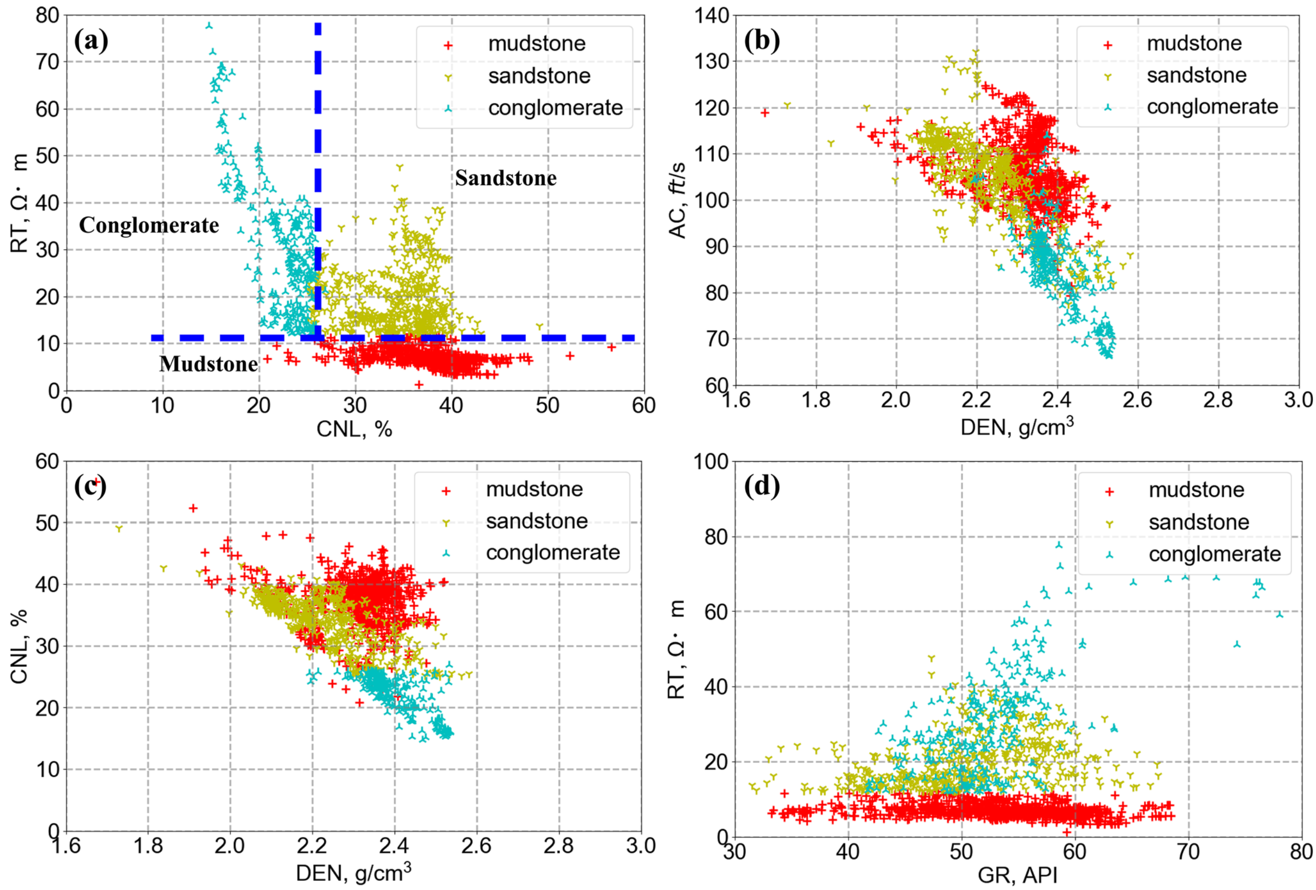

Fig.8 Classification of the logging data to identify lithology

and conglomerate otherwise when RT becomes larger than 11.

It has been found in the literature that a linear relationship exists between the dynamic and static mechanical parameters of geological strata [6–8]

$$E_s = B_1 + K_1 E_d \tag{3}$$

$$\mu_s = B_2 + K_2 \mu_d \tag{4}$$

Where B and K are the coefficients of regressions (dimensionless), μ is the Poisson's ratio (dimensionless), and E is the Young's modulus (Pa). The subscripts s and d stand for "static" and "dynamic," respectively.

Moos and Zoback [52] established the relationship between the unconfined compressive strength (UCS) and the compressional interval velocity (V_p) for coarse-grained sandstone and conglomerate,

$$\mathrm{UCS} = 1.745 \times 10^{-9} \rho V_p^2 + C \tag{5}$$

Where C is the constant that is related to rock (MPa). The relationship between the tensile strength of rock S_t and UCS is

$$S_t = \frac{\mathrm{UCS}}{K}, (K = 8 \sim 15) \tag{6}$$

Where K is an empirical coefficient (dimensionless). Coates et al. [53] proposed an empirical equation to correlate cohesion (S_0) with UCS

$$S_0 = 3.625 \times 10^{-6} UCS \cdot K_d \tag{7}$$

Where S_0 is cohesion (MPa) and K_d is the dynamic bulk modulus of rock (dimensionless). K_d is related to E_d and μ_d in terms of

$$K_d = \frac{E_d}{3(1 - 2\mu_d)} \tag{8}$$

There is a certain relationship between the internal friction angle (φ) and the cohesion of a rock. Chen et al. [54] established the relationship between the cohesion and internal friction angle of sedimentary rock,

$$\begin{cases} \varphi = a \log[M + (M^2 + 1)^{1/2}] + b \\ M = a_1 - b_1 \cdot S_0 \end{cases} \tag{9}$$

Where a, a_1, b, b_1 are constants related to rocks.

Table 3 Dynamic and static elastic parameters of the rock types

Coefficient	B_1 Equation (3) and (4)	K_1	B_2	K_2	C Equation (5)	K Equation (6)	a, a_1, b, b_1 Equation (9)	ξ_1 Equation (11)	ξ_2
mudstone	3.25	0.34	− 0.16	0.97	21	14	a = 2.654 b = 20	1.08	0.96
sandstone	2.89	0.30	0.11	0.95			a_1 = 58.93		
conglomerate	2.66	0.28	0.03	0.72			b_1 = 1.785		

The overburden stress (S_v) at any point of depth z in the crust is estimated by calculating the weight of the strata overlying that point the pore pressure estimation was made using Eaton's method [14]. With assumptions of homogeneous and isotropic linear elastic material for the strata, the horizontal stress can adopt Chen et al. [54] to calculate the maximum and minimum horizontal stresses S_H and S_h,

$$\begin{cases} S_H = \frac{1}{2}[\frac{\xi_1 E_s}{1-v_s} + \frac{v_s(S_v - \alpha P_p)}{1-v_s} + \frac{\xi_2 E_s}{1+v_s}] + \alpha P_p \\ S_h = \frac{1}{2}[\frac{\xi_1 E_s}{1-v_s} + \frac{v_s(S_v - \alpha P_p)}{1-v_s} - \frac{\xi_2 E_s}{1+v_s}] + \alpha P_p \end{cases} \tag{10}$$

In Eq. (10), α is the Biot coefficient. ξ_1 and ξ_2 are the tectonic stress coefficients of the formation. For a specific structural region, the tectonic stress coefficients usually remain constant. Therefore, they can be deduced from known stress values:

$$\begin{cases} \xi_1 = \frac{1}{E_s}[(S_H - S_h - 2\alpha P_p)(1-v_s) - 2v_s(S_v - \alpha P_p)] \\ \xi_2 = \frac{1}{E_s}[(S_H - S_h)(1+v_s)] \end{cases} \tag{11}$$

The coefficients in Eq. (3)-(6) and Eq. (11) need to be determined by correlating the experimental and logging data. For example, in deriving the conversion relation from dynamic to static parameters, the triaxial compression tests were first performed on the cores at different depths to obtain static mechanical parameters. Secondly, the dynamic elastic parameters at the corresponding depths were calculated based on the logging data. Finally, the equation of correlation was established between the dynamic and static parameters. The associated coefficients are listed in Table 3.

3.3 Fracture propagation analysis

In the cohesive zone method, a predefined fracture surface composed of cohesive elements is embedded in the model, where a hydraulic fracture extends along the predefined surface. A traction–separation law controls the fracture process zone (unbroken cohesive zone). Damage initiates when the traction (T) reaches the $T_{max,}$ and the separation (δ) reaches the critical value δ_0. As the T increases, δ decreases due to material degradation (Fig. 9). Once δ reaches the displacement at failure (δ_f), the T reduces to zero, and the cohesive elements are broken. The traction–separation law is no longer valid in the fluid-filled fracture zone (broken cohesive zone). The mathematic crack tip refers to the point, which is yet to separate, while the cohesive crack tip represents the position where the T reaches the cohesive strength T_{max}. The material crack tip is when the material completely fails with δ equal to δ_f.

To evaluate the degradation of a material subject to mechanical loading, a damage initiation criterion [56] can be used:

$$\left\{\frac{\langle T^n \rangle}{T_0^n}\right\}^2 + \left\{\frac{T^s}{T_0^s}\right\}^2 + \left\{\frac{T^t}{T_0^t}\right\}^2 = 1 \tag{12}$$

Where T^n represents the normal traction and T^s and T^t are shear tractions in the first and second direction, respectively. ${T_0}^n$, ${T_0}^s$, and ${T_0}^t$ represent the corresponding peak values of the nominal stress or the shear stresses at the two perpendiculars. The symbol " $< >$ " represents a pure compressive deformation or stress state before any damage of the material occurs.

A bilinear cohesive traction–separation law can be expressed as follows [55],

$$T = \begin{cases} K_0\delta & 0 \le \delta^{max} \le \delta_0 \\ (1-D)K_0\delta & \delta_0 \le \delta^{max} \le \delta_f \\ 0 & \delta^{max} \ge \delta_f \end{cases} \tag{13}$$

Where K_0 is the initial stiffness of the cohesive interface (Pa), δ^{max} is the maximum value of the separation attained during the loading history (m), and the scalar damage variable D represents the overall damage in the material (dimensionless), which can be expressed as,

$$D = \frac{\delta_f(\delta^{max} - \delta_0)}{\delta^{max}(\delta_f - \delta_0)} \tag{14}$$

The fluid constitutive response comprises the tangential flow along the direction of the fracture propagation and the normal flow perpendicular to the fracture surface. The fluid is assumed to be incompressible and follows the Newtonian rheology. The tangential flow is governed by the lubrication equation [55],

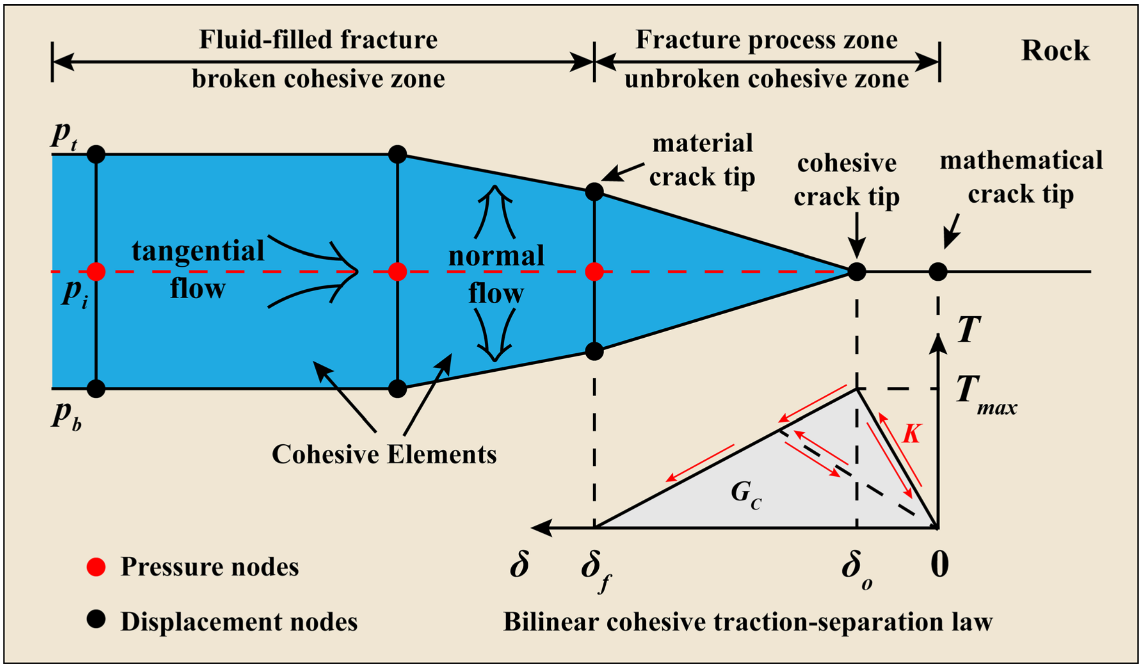

Fig. 9 Cohesive zone hydraulic fracture model and bilinear cohesive traction–separation law (modified from [55])

$$q = \frac{w^3}{12\mu}\nabla p \tag{15}$$

Where q is the fluid flux of the tangential flow (m^3/s), ∇p is the fluid pressure gradient along the fracture (Pa), μ is the fluid viscosity (mPa·s), and w is the fracture aperture (m).

The normal flow is the fluid exchange between the fracture surface and the surrounding rock. It is defined as follows [55]

$$\begin{cases} q_t = c_t(p_i - p_t) \\ q_b = c_b(p_i - p_b) \end{cases} \tag{16}$$

Where q_t and q_b are the flow rates into the top and bottom surfaces (m^3/s), respectively; p_b is the midface pressure (m^3/s); p_t and p_b are the pore pressure in the surrounding porous rock on the top and bottom surfaces of the fracture (Pa), respectively; c_t and c_b define the corresponding fluid leak-off coefficients (dimensionless).

The equation of mass conservation is expressed as [37]

$$\frac{\partial w}{\partial t} + \nabla \cdot q + (q_t + q_b) = Q(t)\delta(x, y) \tag{17}$$

Substituting Eq. (15) and (16) in Eq. (17) results in Reynold's lubrication equation. Therefore, a coupled fluid pressure-traction-separation relationship holds for the cohesive zone, which is defined by the traction-separation law and the pressurized fracture,

$$\frac{\partial w}{\partial t} + c_t(p_f - p_t) + c_b(p_f - p_b) = \frac{1}{12\mu}\nabla \cdot (w^3 \nabla p_f) + Q(t)\delta(x, y) \tag{18}$$

During the process of hydraulic fracturing, the flow of fracturing fluid and the deformation of the rock matrix interact and influence each other: (1) The deformation of the rock will cause changes in the pore volume and its structure, subsequently affecting the pressure evolution; (2) the change in pore pressure leads to modification of effective stresses. The equilibrium equation in the form of

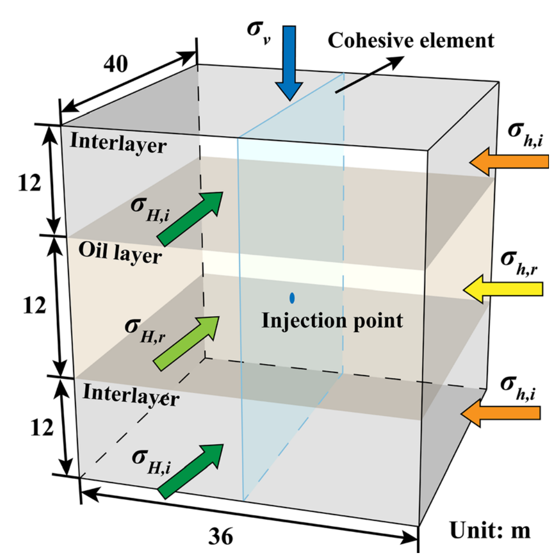

Fig.10 Three-dimensional configuration of the cohesive zone model

Table 4 Parameters used for the CZM fracture models

(a) Formation physical parameters					
Layer	Permeability, K (mD)	Porosity, ϕ (%)	Elasticity modulus, E (GPa)	Poisson's ratio, μ (-)	
Oil layer	200	15	12	0.21	
Interlayer	10	5	20	0.25	
(b) Cohesive zone properties					
Layer	Tensile strength, T (MPa)	Specific thickness, t (m)	Fracture energy, G_C (kPa·m)	Leak-off coefficient, c (m/kPa·s)	Cohesive stiffness, K_n (GPa)
Oil layer	2	0.001	4000	1E-12	12
Interlayer	3	0.001	5000	1E-13	20
(c) In situ stress field (effective)					
Layer	Overburden stress, S_v (MPa)	Maximum horizontal stress, S_H (MPa)	Minimum horizontal stress, S_h (MPa)	Difference of minimum horizontal stress, ΔS_h (MPa)	
Oil layer	29	30	24	0/2/4	
Interlayer		30/32/34	24/26/28		
(d) Fluid properties					
	Injection rate, q (m^3/min)	Viscosity, v (mPa.s)		Weight, g (kN/m^3)	
Fracturing fluid	1/3/5	1/50/100		980	

a virtual work principle for volume can be written as follows:

$$\int_V (\sigma' - p_w I)\delta\varepsilon \mathrm{dV} = \int_S t \cdot \delta v \mathrm{dS} + \int_V f \cdot \delta v \mathrm{dV} \tag{19}$$

Where σ' is the mean effective stress (Pa), p_w is the pore pressure (Pa), and δ_ε and δ_v are the virtual strain rate matrix and virtual velocity (dimensionless), respectively; t and f are the surface traction and body force per unit volume (N), respectively; and I is the unit matrix.

The continuity equation of fluid seepage is expressed as follows:

$$\frac{1}{J}\frac{\partial}{\partial t}(J\rho_w n_w) + \frac{\partial}{\partial x}(\rho_w n_w v_w) = 0 \tag{20}$$

Where J is the porous media volume change ratio (dimensionless), ρ_w is the mass density of the liquid (g/cm^3), n_w is the porosity of the medium (dimensionless), v_w is the average velocity of the liquid relative to the solid phase (mPa·s), and x is the space vector.

Darcy's law is adopted to describe the fluid low in the rock medium:

$$v_m = -\frac{1}{n_w g \rho_w} k \cdot \left(\frac{\partial p_w}{\partial x} - \rho_w g\right) \tag{21}$$

Where k is the rock permeability vector (m^2) and g is the gravitational acceleration vector (m/s^2).

The geometry of the three-dimensional mechanical earth model is displayed in Fig. 10. The model is composed of an oil layer (sandy conglomerate) sandwiched by an upper and a lower mudstone interlayer. A vertical cohesive interface was preset as the middle plane of the model, along which the hydraulic fracture will propagate through the layer interfaces. The 12-node displacement and pore pressure cohesive element (COH3D8P) and the 8-node linear hexahedral element (C3D8P) were assigned to the hydraulic fracture and the surrounding medium, respectively [55]. The soil module in the ABAQUS platform was applied for the hydraulic and mechanical coupled simulation. User subroutines were written to prescribe the initial field variables and the nonuniform in situ stress boundary conditions.

The influences of the ΔS_h, fracturing fluid viscosity, and injection rate on the vertical fracture propagation were evaluated using the above geomechanical and fracture models. Table 4 lists the parameters used for the two models.

4 Results and discussion

4.1 In situ stress field

Well T002 is located at the eastern part of the No.7 region, passing through a formation that has a gentle dip angle. Because of the abundant geological information, Well 2 was selected as the benchmark for the following stress analysis. Figure 11 shows the rock mechanics and in situ stress profile of Well T002. The colored scatter points represent Young's modulus and Poisson's ratio measured by the laboratory triaxial experiments and in situ stress by

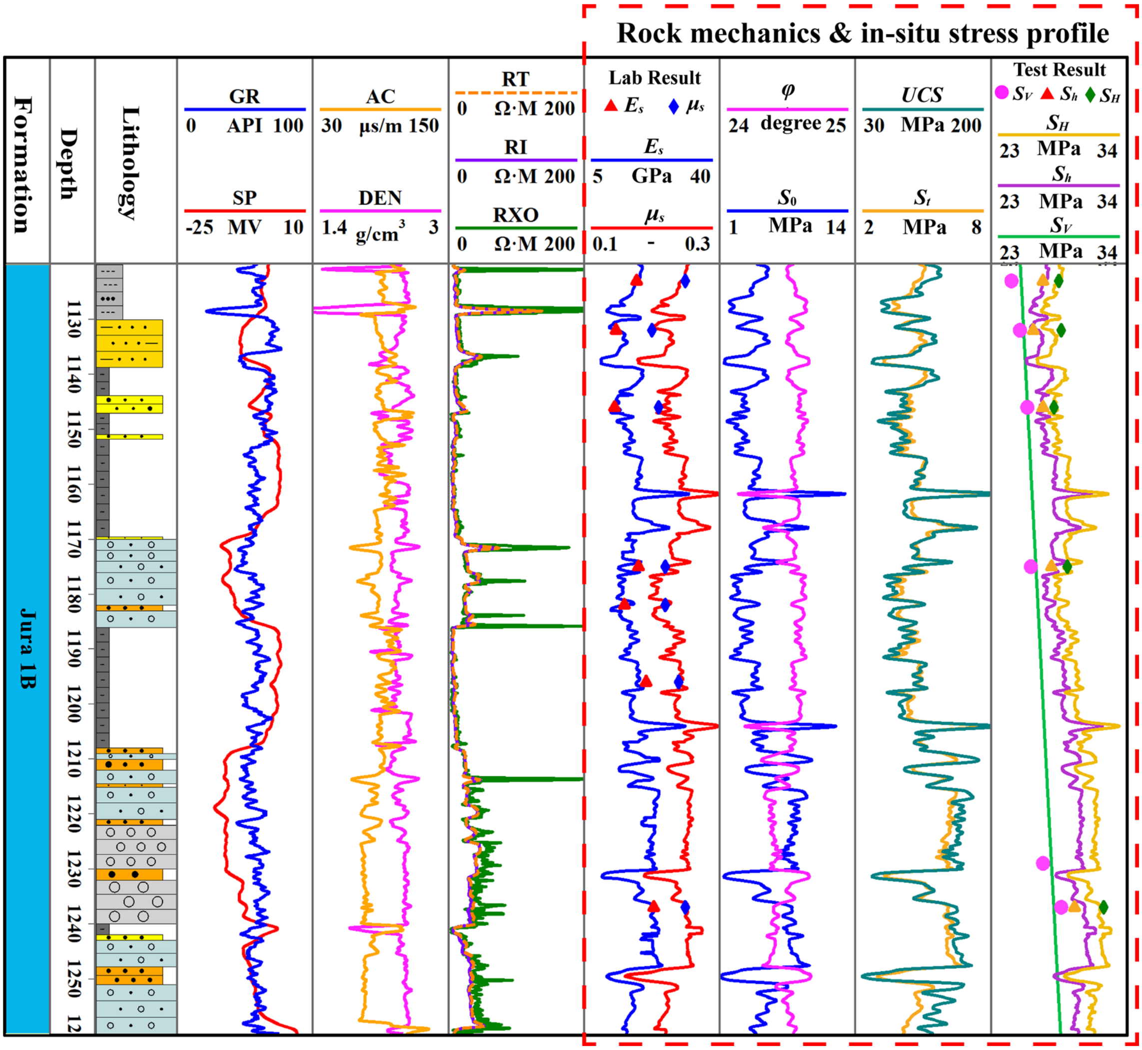

Fig. 11 Rock mechanics and in situ stress profile of well T002

the Kaiser stress tests. It is found from Fig. 11 that the experimental data are in good agreement with the calculated results. Also, S_v is identified as the minimum principal stress (last column) for most deep ranges, leading to horizontal fractures upon hydraulic fracturing. However, for some specific depths, such as at 1140 m and 1250 m, S_h becomes the minimum principal stress. In this case, the hydraulic fracture propagates in the vertical direction.

Applying the methods introduced in Sect. 3, the stress profile of 368 wells in the studied region was produced. Therefore, the three-dimensional in situ stress field of the studied formation was constructed using the Kriging method [57]. Figure 12 shows the three-dimensional distribution of pore pressure and in situ stress in the $J_1b_4{}^{1-2}$ sand body of the Badaowan formation. If the layer velocity data are obtained, what method can be used for further interpolation to obtain a spark field with a more obvious physical meaning.

Figure 13 is a three-dimensional field distribution of the stress difference ΔS ($S_v - S_h$) of the $J_1b_4{}^{1-2}$ sand body in Badaowan formation. The value of ΔS is used to determine the minimum principal stress. Because hydraulic fractures usually propagate perpendicular to the direction of minimum stress, when $\Delta S > 0$ (i.e., $S_v > S_h$), hydraulic fractures propagate in the vertical direction, and when $\Delta S < 0$ ($S_v < S_h$), hydraulic fractures are horizontal fractures. In the warm-colored region (yellow to red), the hydraulic fractures would propagate in the vertical direction. In the green to blue region, tending to create horizontal fractures upon hydraulic fracturing.

4.2 Vertical HF propagation morphology

Figure 14 shows the vertical fracture morphology at different magnitudes of ΔS_h. When ΔS_h equals zero, a hydraulic fracture propagates in the vertical direction and

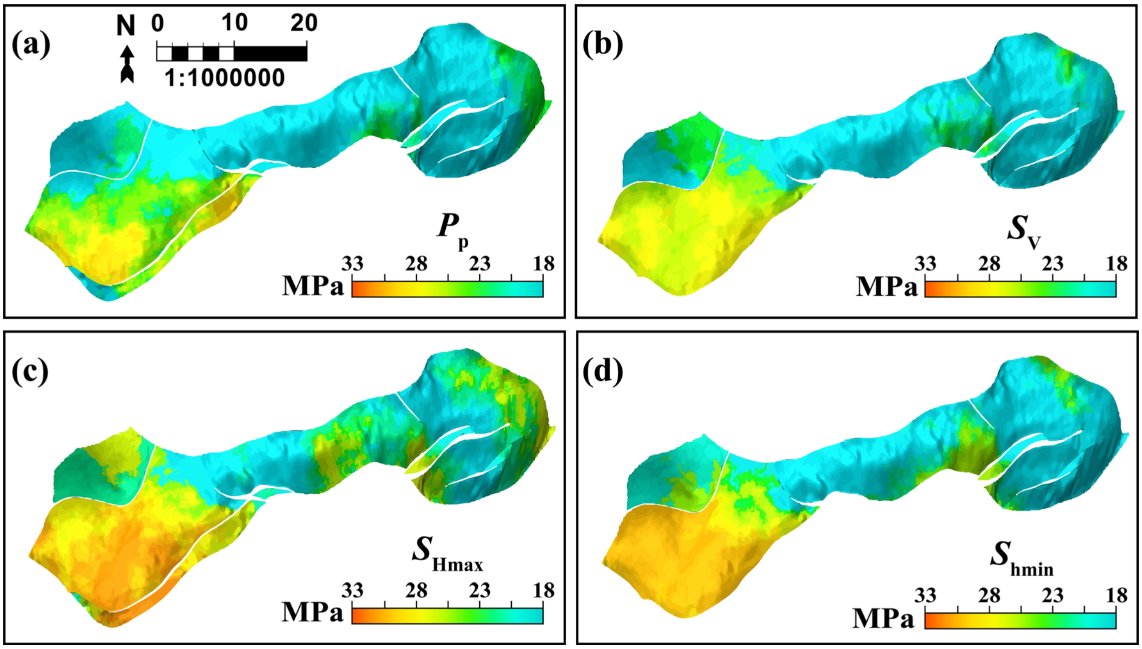

Fig.12 Three-dimensional in situ stress field of the $J_1b_4.^{1-2}$ sand body

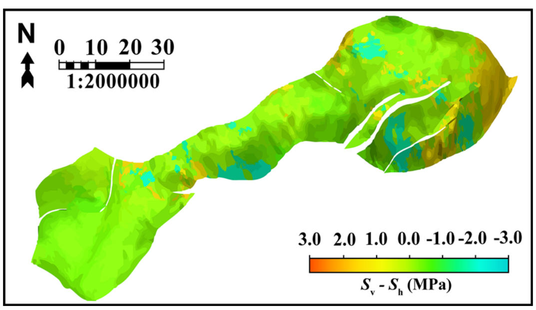

Fig.13 The field distribution of the stress difference $S_v - S_h$ of the $J_1b_4.^{1-2}$ sand body

Table 5 Hydraulic fracture parameters under different ΔS_h magnitudes

ΔS_h (MPa)	l, Length (m)	h, Height (m)	l / h (−)
0	30.8	21.3	1.44
2	33.1	17.9	1.85
4	37.4	12.0	3.12

enters the interlayer. Although the ΔS is zero, the fracture length still develops a length of 30.8 m, being larger than its height of 21.3 m. The major reason for such a phenomenon lies in the fact that the leak-off volume is dependent on the permeability of the formation. Because the permeability of the oil layer is much higher than that of the interlayer, the former acts as a preferred fluid flow path

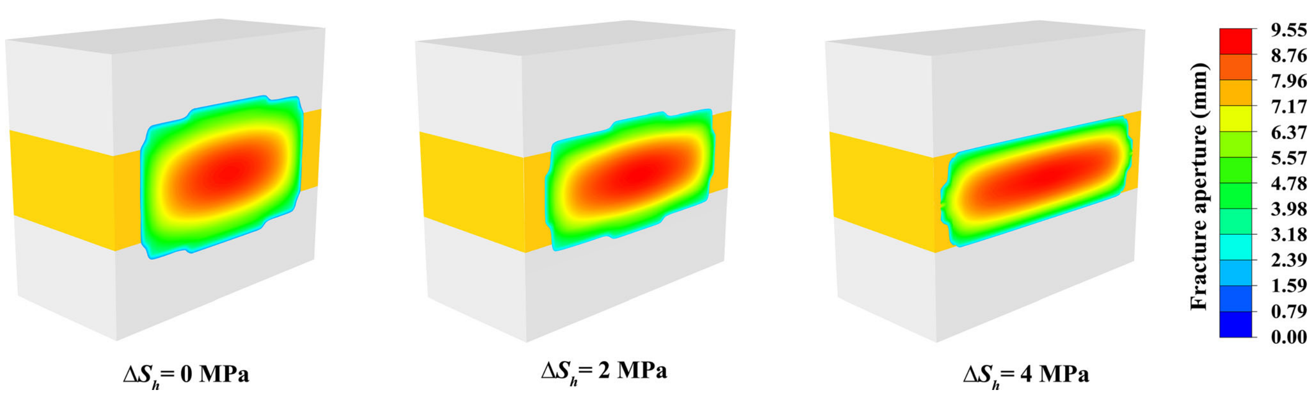

Fig.14 Hydraulic fracture morphology under different ΔS_h magnitudes

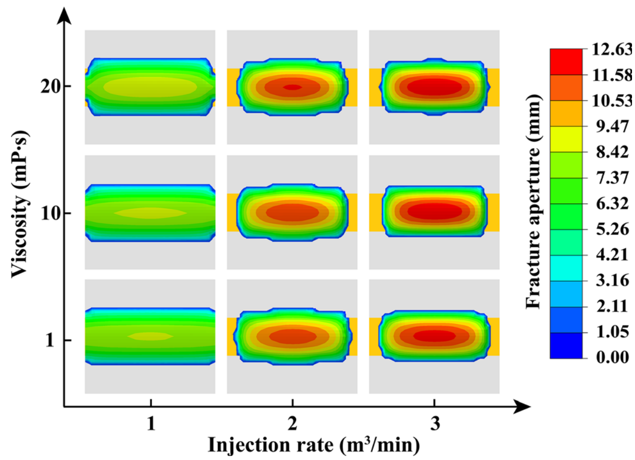

Fig.15 Hydraulic fracture morphology given different viscosity and injection rate

from the fracture to the formation matrix. Therefore, hydraulic fracture develops a higher tendency to extend to the oil layer instead of to the interlayer. When ΔS_h becomes 2 MPa, the height of the fracture decreases significantly to merely 17.9 m while the fracture length increases to 33.1 m. As ΔS_h reaches 4 MPa, the hydraulic fracture is mostly constrained in the oil layer, generating a fracture height of merely 12 m. Table 5 lists the geometric properties of a hydraulic fracture under different ΔS_h magnitudes. As the ΔS_h increases, it is more difficult for the fracture to propagate vertically. It must be noted that 4 MPa serves as the upper limit but not the critical value for fracture penetration to the interlayer. If ΔS_h becomes greater than 4 MPa, the vertical fracture shall be constrained in the oil layer. Only when ΔS_h becomes smaller than 4, MPa can fracture be possibly enter the interlayer. If there are natural fractures in the formation, even when ΔS_h gets smaller than 4 MPa, the fractures may connect to the natural fractures and not extend to the interlayer. In this sense, further studies are desired to determine the lower limit of fracture penetration.

The CMZ model was further used to evaluate fracturing fluid viscosity and injection rate influences on the hydraulic fracture morphology. The total fluid injection volume was identical to the case in Fig. 15. It can be seen from the figure that the injection rate and viscosity have a significant effect on the fracture geometry. It also shows that the middle part of the fracture extends further upward or downward because it is closer to the injection point reaching the fracture pressure of the interlayer.

Figure 16a shows the effect of different injection rates on the fracture height. The fracture height decreases as the injection rate increases, but its aperture goes up. At a constant injection rate, the viscosity has a negligible effect on the fracture height but imposes a negative impact on the aperture (Fig. 16b and c). When the viscosity is low, more fluid could enter the oil layer and the interlayer, increasing pore pressure and decreasing fracture pressure. Therefore, the fracture height and length are more extensive than that of high viscosity. When the injection rate increases, the time required to inject the same volume of fracturing fluid is shorter. Currently, the leak-off of fracturing fluid is small, leading to the height and length of fracture which are smaller than those of the low injection rate.

4.3 Field validation

The fracture morphology of well T009 was analyzed to validate the methods proposed in this study. Well T009 is a vertical well located in the eastern part of the No.7 region. The buried depth of the oil layer is 890–900 m, whose upper part is a muddy interlayer with low permeability. The in situ stress analysis reveals that the minimum principal stress is S_h. In addition, the ΔS_h is about 2 MPa, implying that a hydraulic fracture can propagate upwards and enter the interlayer.

To detect the vertical fracture before and after fracturing, cross-dipole shearing wave logging was implemented in Well T009 and provided the results in Fig. 17. An important application of the four-component cross-dipole logging is the analysis of formation anisotropy [58]. The second and third tracks of Fig. 17 show the average anisotropy from the transmitter to the receiver before and after fracturing. The fourth and fifth tracks display the reflector image before and after fracturing, respectively. Hydraulic fractures can create azimuthal shear-wave anisotropy around the borehole. The amount of anisotropy gives an indication of fracture intensity, and the associated fast-shear polarization azimuth gives the strike of open fractures [59]. The dipole acoustic source–receiver system can radiate and receive shear waves to and from remote geologic reflectors in the formation, thus potentially allowing for imaging geological features, such as fractures, faults, and bed boundaries [60, 61]. After fracturing, the reflector imaging (RFIMG) of the shear wave shows that the formation signal above the perforation section (rectangle B) becomes enhanced. This implies that the fracture has extended upward to the overlying interlayer. The imaging results identify a fold structure (yellow and red parts) in the vicinity of the wellbore. In addition, the anisotropy of the perforation section (marked by rectangle A) and the interlayer (rectangle C) got strengthened. It further indicates that the hydraulic fracture has extended upward by 20 m to reach a shallower depth of 870 m. Such a phenomenon also implies that the hydraulic fractures intruded the upper interlayers.

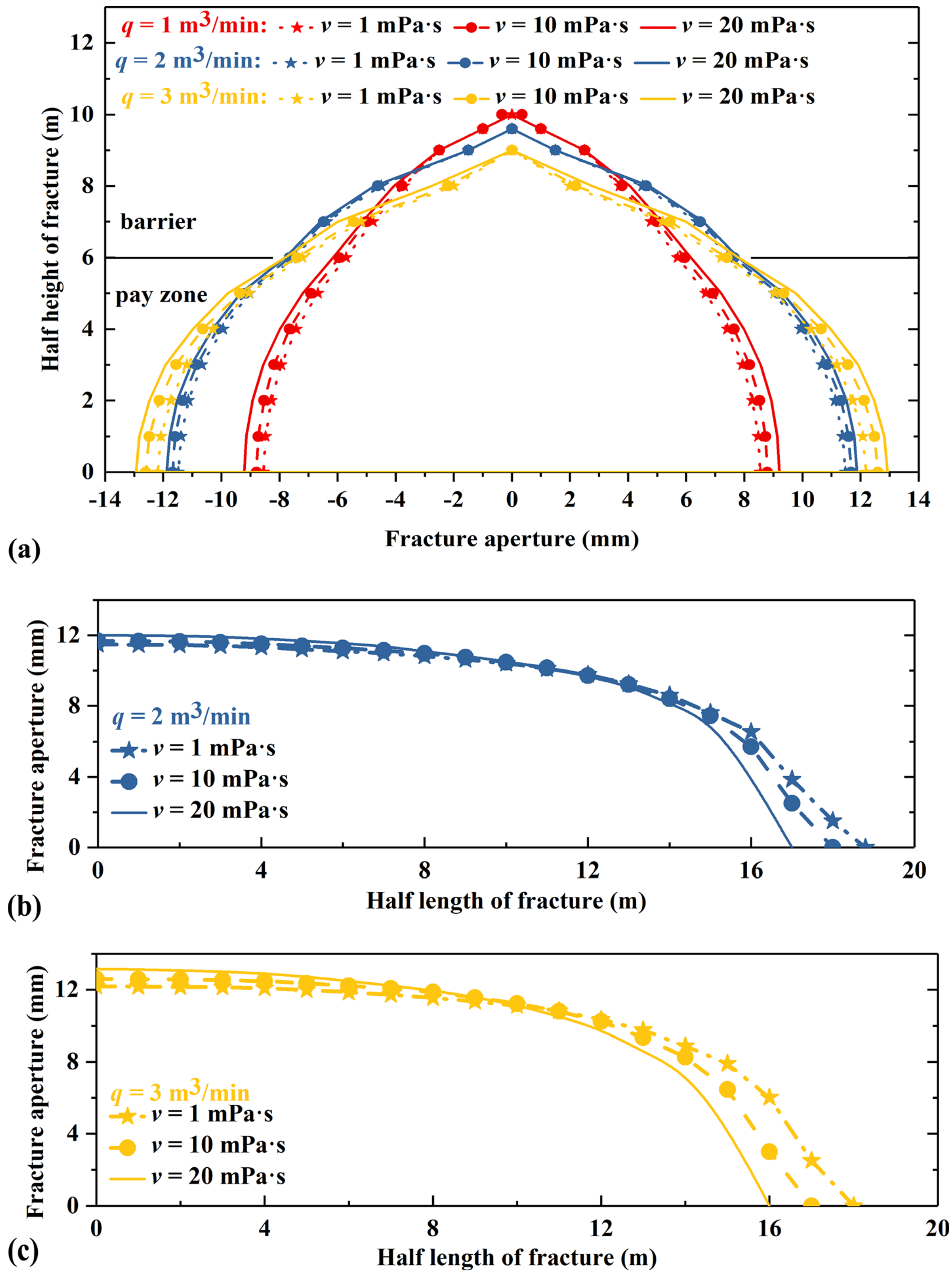

Fig.16 Influences of fracturing fluid viscosity and injection rate on fracture morphology

4.4 Method to estimate hydraulic fracture morphology

The fracture morphology of the No.7 region Badaowan formation can be classified into four types: (1) When S_v is greater than S_h, horizontal fractures tend to develop (Fig. 18a); (2) when S_v is less than S_h and ΔS_h is greater than 4 MPa, the vertical fracture will be constrained in the oil layer (Fig. 18 (b)). (3) When S_v is smaller than S_h, and only ΔS_h gets smaller than 4 MPa, a fracture may extend to the interlayer (Fig. 18c); (4) an increase in the injection rate would reduce the height of the fracture (Fig. 18d).

A schematic approach to estimate the fracture propagation behavior of the Badaowan formation in No.7 region can therefore be proposed (Fig. 18). First, given the location of the new well to be stimulated, the in situ stress field

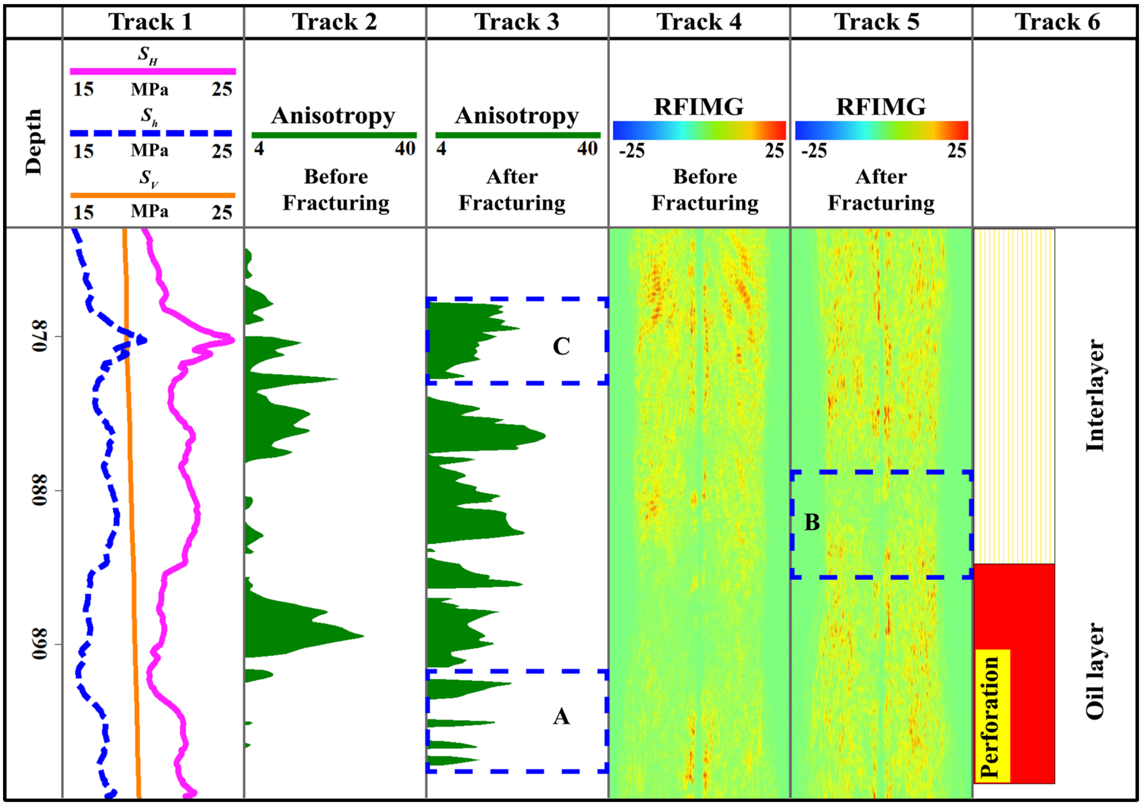

Fig.17 Cross-dipole shear wave logging profile in well T009

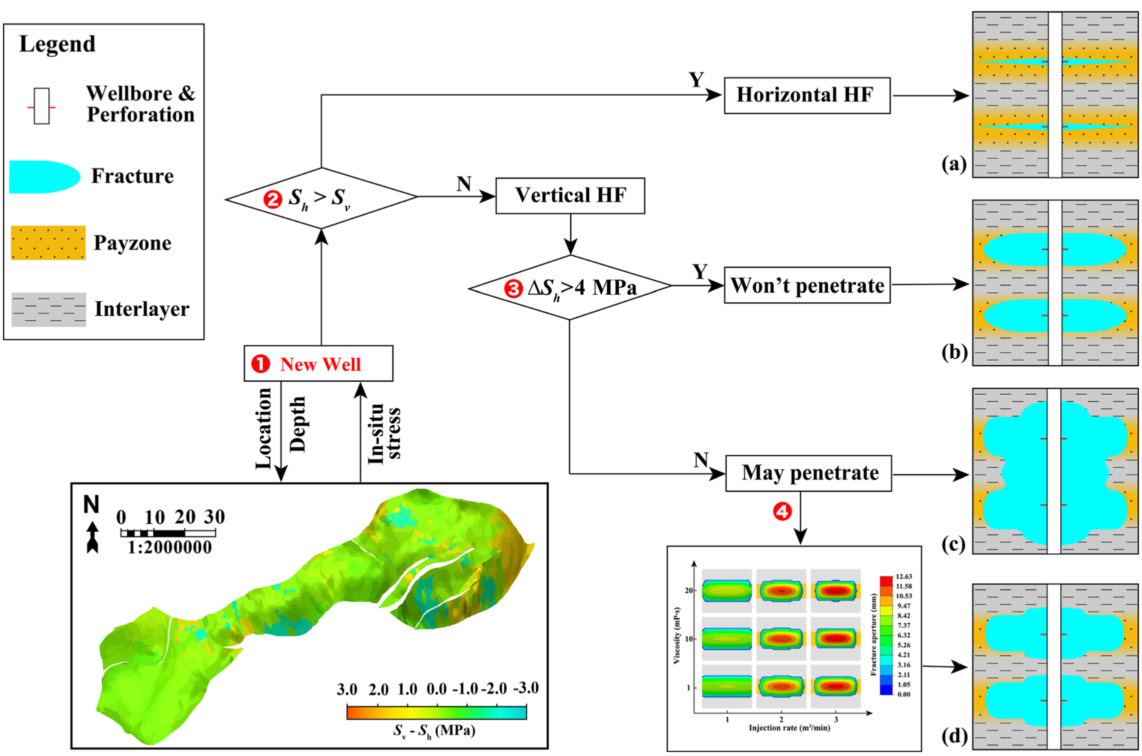

Fig.18 Schematic diagram of fracture morphology of the No.7 region Badaowan formation

can be established. Secondly, whether the hydraulic fracture initiates in the horizontal or vertical direction can be evaluated based on the magnitude of $S_h - S_v$. Afterward, if the hydraulic fracture is identified to be a vertical one, the magnitude of ΔS_h could be calculated to determine whether the fracture would propagate into the interlayer. Finally, the fracture height and aperture are evaluated by implementing different viscosities and injection rates of the fracturing fluid.

5 Summary and conclusions

This paper constructed the three-dimensional distribution of in situ stress of the Badaowan formation in the No.7 region and further proposed a systematic method to evaluate the morphology of hydraulic fractures under different in situ stress and engineering circumstances. Several conclusions can be drawn as follows.

1. The tectonic activities in geological history produced a complex pattern of the in situ stress field. The maximum horizontal stress S_H distributes at an azimuth close to NW 82°. For most regions, the stress components display a relation as $S_H > S_h > S_v$, where a horizontal fracture tends to develop upon fracturing. In the central and southeastern part of the region, the stresses follow a relation of $S_H > S_v > S_h$, where vertical fractures are dominant.
2. The minimum horizontal stress difference ΔS_h between the oil and the interlayer plays the most significant role in affecting the vertical extension of the fracture in a given formation. The results of this study show that an increase in ΔS_h suppresses the transverse extension of the fracture. When ΔS_h becomes greater than 4 MPa, the vertical fracture will be constrained in the oil layer.
3. As the fluid injection rate increases, the height of a fracture decreases, and the width increases. The viscosity has negligible effect on the fracture height, but its increase will enlarge the fracture width and decrease the fracture length. The height of a vertical fracture can therefore be adjusted by making the proper design of the viscosity and injection of the fracturing fluid.
4. The systematic method proposed in this study can characterize the stress field and the configuration of a hydraulic fracture in details. The findings can help field engineers estimate the fracture morphology after fracturing to design an optimum fracturing plan. Future research will be dedicated to investigating the influences of the interfacial strength, natural fractures, petrophysical heterogeneity, and other engineering factors on the vertical fracture propagation such that a more refined fracture morphology description can be derived.

Acknowledgements The author would like to acknowledge the financial support provided by China's National Major Science and Technology Projects (Grant No. 2017ZX05009-003) and China Scholarship Council. Gratitude is also attributed to the Xinjiang Oilfield Corporation for providing us with the in situ cores and the field data.

Declaration

Conflict of interest The authors declare that they have no known competing financial interests or personal relationships that could have appeared to influence the work reported in this paper.

References

1. Hubbert MK, Willis DG (1957) Mechanics of hydraulic fracturing. Petr Trans AIME. https://doi.org/10.2118/686-G
2. Abass HH, Hedayati S, Meadows DL (1992) Nonplanar fracture propagation from a horizontal wellbore: experimental study. SPE Ann Tech Conf Exh. https://doi.org/10.2118/24823-PA
3. Zoback MD (2007) Reservoir geomechanics. Cambridge University Press, UK
4. Zhang L, Cao P, Radha K (2010) Evaluation of rock strength criteria for wellbore stability analysis. Int J Rock Mech Min Sci 47(8):1304–1316. https://doi.org/10.1016/j.ijrmms.2010.09.001
5. Mavko G, Mukerji T, Dvorkin J (1998) The rock physics handbook, 1 sted. Cambridge University Press, Cambridge
6. King MS (1983) Static and dynamic elastic properties of rocks form the Canadian shield. Int J Rock Mech Min Sci Geomech. 20(5):237–241. https://doi.org/10.1016/0148-9062(83)90004-9
7. Brautigam T, Knochel A, Lehne M (1998) Prognosis of uniaxial compressive strength and stiffness of rocks based on point load and ultrasonic tests. Otto-Graf-J 9:61–79
8. Al-Tahini A (2003) The effect of cementation on the mechanical properties for jauf reservoir at Saudi Arabia. University of Oklahoma, Norman
9. Eissa EA, Kazi A (1988) Relation between static and dynamic Young's moduli of rocks. Int J Rock Mech Mining Sci 25(6):479–482
10. Wang HF (2000) Theory of linear poroelasticity with applications to geomechanics and hydrogeology. Princeton NJ. Princeton University Press, New Jerssy, p 304
11. Eaton BA (1969) Fracture gradient prediction and its application in oilfield operations. J Pet Technol 246:1353–1360. https://doi.org/10.2118/2163-PA
12. Thiercelin M, Plumb R (1994) A core-based prediction of lithologic stress contrasts in east texas formations. SPE Form Eval 9(04):251–258. https://doi.org/10.2118/21847-PA
13. Bratton T, Bornemann T, Li Q, Plumb R, Rasmus J, Krabbe H (1999) Logging-whiledrilling images for geomechanical, geological and petrophysical interpretations. In: The 40th Annual Logging Symposium, SPWLA, Oslo, Norway. May 30– June 3. SPWLA-1999-JJJ
14. Chen M, Jin Y, Zhang GQ (2008) Rock mechanics in petroleum engineering. Science Press, Beijing
15. Zhang YS, Zhang JC, Yuan B et al (2018) In-situ stresses controlling hydraulic fracture propagation and fracture breakdown pressure. J Pet Sci Eng 164:164–173. https://doi.org/10.1016/j.petrol.2018.01.050

16. Warpinski NR, Teufel LW (1989) In-situ stresses in low permeability, nonmarine rocks. J Pet Technol 41(4):405–414. https://doi.org/10.2118/16402-PA
17. Miller WK II, Peterson RE, Stevens JE, Lackey CB, Harrison CW (1994) In-situ stress profiling and prediction of hydraulic fracture azimuth for the West Texas Canyon Sands formation. SPE Prod Facil 9(3):204. https://doi.org/10.2118/21848-PA
18. Wileveau Y, Cornet FH, Desroches J, Plumling P (2007) Complete in situ stress determination in an argillite sedimentary formation. Phys Chem Earth 32:866–878. https://doi.org/10.1016/j.pce.2006.03.018
19. Labudovic V (1984) The effect of poisson's ratio on fracture height. J Pet Technol 36(2):287–290. https://doi.org/10.2118/10307-PA
20. Li CH, Chen M, Jin Y (2002) Experimental study on hydraulic fracturing of layered media. In: The Seventh Academic Conference of Chinese Society of Rock Mechanics and Engineering, Xi'an, China
21. Tan P, Jin Y (2017) Analysis of hydraulic fracture initiation and vertical propagation behavior in laminated shale formation. Fuel 206:482–493. https://doi.org/10.1016/j.fuel.2017.05.033
22. Zhang GM, Liu H, Zhang J et al (2010) Three-dimensional finite element simulation and parametric study for horizontal well hydraulic fracture. J Petrol Sci Eng 72(3–4):310–317. https://doi.org/10.1016/j.petrol.2010.03.032
23. Warpinski NR, Clark JA, Schmidt RA et al (1982) Laboratory investigation on the effect of in-situ stresses on hydraulic fracture containment. Int J Rock Mech Mining Sci Geomech Abstr 19(6):333–340. https://doi.org/10.2118/9834-PA
24. Teufel LW, Clark JA (1984) Hydraulic fracture propagation in layered rock: experimental studies of fracture containment. SPE J 24(01):19–32. https://doi.org/10.2118/9878-PA
25. Warpinski NR, Schmidt RA, Northrop DA (1982) In-situ stresses: the predominant influence on hydraulic fracture containment. J Pet Technol 34(03):653–664. https://doi.org/10.2118/8932-PA
26. Fisher K, Warpinski NR (2011) Hydraulic fracture-height growth: real data. SPE Annual Tech Conf Exhib Denver Colo USA. https://doi.org/10.2118/145949-PA
27. Jin Y, Chen M, Zhou J, Geng YD (2008) Experimental study on the effects of salutatory barrier on hydraulic fracture propagation of cement blocks. ACTA PETROLEI SINICA 29(2):300–303
28. Warpinski NR, Teufel LW (1987) Influence of geologic discontinuities on hydraulic fracture propagation. J Pet Technol 39(2):209–220. https://doi.org/10.2118/13224-PA
29. Hossain MM, Rahman MK (2008) Numerical simulation of complex fracture growth during tight reservoir stimulation by hydraulic fracturing. J Pet Sci Eng 60(2):86–104. https://doi.org/10.1016/j.petrol.2007.05.007
30. Rahman MM, Hossain MM, Crosby DG et al (2002) Analytical, numerical and experimental investigations of transverse fracture propagation from horizontal wells. J Pet Sci Eng 35(3):127–50. https://doi.org/10.1016/S0920-4105(02)00236-X
31. Tan P, Jin Y, Pang HW (2021) Hydraulic fracture vertical propagation behavior in transversely isotropic layered shale formation with transition zone using XFEM-based CZM method. Eng Fract Mech. https://doi.org/10.1016/j.engfracmech.2021.107707
32. Zhang F, Dontsov E, Mack M (2017) Fully coupled simulation of hydraulic fracture interacting with natural fractures with a hybrid discrete-continuum method. Int J Numer Anal Methods Geomech 41(13):1430–1452. https://doi.org/10.1002/nag.2682
33. Zhang F, Damjanac B, Maxwell S (2019) Investigating hydraulic fracturing complexity in naturally fractured rock masses using fully coupled multiscale numerical modeling. Rock Mech Rock Eng 52(12):5137–5160. https://doi.org/10.1007/s00603-019-01851-3
34. Barenblatt GI (1962) The mathematical theory of equilibrium of cracks in brittle fracture. Adv Appl Mech 7:55–129. https://doi.org/10.1016/S0065-2156(08)70121-2
35. Dugdale DS (1960) Yielding of steel sheets containing slits. J Mech Phys Solids 8(2):100–104. https://doi.org/10.1016/0022-5096(60)90013-2
36. Chen Z (2012) Finite element modelling of viscosity-dominated hydraulic fractures. J Pet Sci Eng 88–89:136–144. https://doi.org/10.1016/j.petrol.2011.12.021
37. Yao Y, Liu L, Keer LM (2015) Pore pressure cohesive zone modeling of hydraulic fracture in quasi-brittle rocks. Mech Mater 83:17–29. https://doi.org/10.1016/j.mechmat.2014.12.010
38. Chen Z, Jeffery R, Zhang X (2015) Numerical modeling of three-dimensional T-Shaped hydraulic fractures in coal seams using a cohesive zone finite element model. Hydraul Fract J 2(2):20–37
39. Chen Z, Bunger AP et al (2009) Cohesive zone finite element-based modeling of hydraulic fractures. Acta Mech Solida Sin 22(5):443–452. https://doi.org/10.1016/S0894-9166(09)60295-0
41. Guo J, Luo B, Lu C, Lai J, Ren J (2017) Numerical investigation of hydraulic fracture propagation in a layered reservoir using the cohesive zone method. Eng Fract Mech 186:195–207. https://doi.org/10.1016/j.engfracmech.2017.10.013
42. Nolte KG (1979) Determination of fracture parameters from fracturing pressure decline. SPE. https://doi.org/10.2118/8341-MS
43. Nolte KG, Maniere JL, Owens KA (1997) After-closure analysis of fracture calibration tests. SPE. https://doi.org/10.2118/38676-MS
44. Barree RD, Mukherjee H (1996) Determination of Pressure dependent Leakoff and Its Effects on Fracture Geometry. The SPE Annual Technical Conference and Exhibition, Denver, Colorado, USA SPE. https://doi.org/10.2118/36424-MS
45. Barree RD (2000) Adapting high permeability leakoff analysis to low permeability sands for estimating reservoir engineering parameters. The SPE Rocky Mountain Regional/Low Permeability Reservoirs Symposium, Denver, Colorado, USA SPE. https://doi.org/10.2118/60291-MS
46. iStress, (2021) Manual for determining the minimum horizontal stress following the G function method. China, HNSH Corp, Chengdu
47. Hickman SH, Zoback MD (1983) The interpretation of hydraulic fracturing pressuretime data for in situ stress determination. National Academy Press, Washington, D.C, Hydraulic Fracturing Measurements
48. Fjaer E, Holt RM, Horstrud M et al (2008) Petroleum related rock mechanics, 2nd edn. Elsevier, Amsterdam
49. Wagner D, Muller B, Tingay M (2004) Correcting for tool decentralization of oriented six-arm caliper logs for determination of contemporary tectonic stress orientation. Petrophysics 45(6):530–539
50. Wang Z (2000) Dynamic versus static elastic properties of reservoir rocks. J Seismic Acoustic Velocities Reservoir Rocks 3:531–539
51. Asef MR, Farrokhrouz M (2017) A semi-empirical relation between static and dynamic elastic modulus. J Petrol Sci Eng 157:359–363. https://doi.org/10.1016/j.petrol.2017.06.055
52. Rider MH, Kennedy M (2011) The Geological Interpretation of Well Logs 3rd, revised. Rider-French Consulting Limited. Whittles Publishing Dunbeath, Scotland, pp 131–134
53. Moos D, Zoback MD et al (1999) Feasibility study of the stability of openhole multilaterals. 1999 SPE Mid-continent Operations Symposium, Oklahoma City, Society of Petroleum Engineers, Cook Inlet, Alaska. https://doi.org/10.2118/73192-PA
54. Coates GR, Denoo SA (1981) Mechanical properties program using borehole analysis and Mohr's Circle. In: SPWL A 22nd

Annual logging symposium strans actions SPWLA-1981-DD. OnePetro: urban
55. Chen M, Jin Y, Zhang GQ (2008) Rock mechanics in petroleum engineering. Science Press, Beijing
56. Eaton BA (1975) The equation for geopressure prediction from well logs. Soc Pet Eng AIME SPE. https://doi.org/10.2118/5544-MS
57. ABAQUS, 2014. Abaqus theory guide, version 6.14, Dassault Systèmes Simulia Corp, Providence, RI USA
58. Camanho PP, Davila CG (2002) Mixed-mode decohesion finite elements for the simulation of delamination in composite materials NASA/TM-2002–211737. pp:1–42
59. Qiao GR, Cai HW, Zhou AN et al (2016) Coal quality prediction model of drilling coal based on kriging interpolation method. Coal Technol 35(02):151–153
60. Dillen MWP, Cruts HMA, Groenenboom J et al (1999) Ultrasonic velocity and shear-wave splitting behavior of a Colton sandstone under a changing triaxial stress. Geophysics 64(5):1603–1607. https://doi.org/10.1190/1.1444664
61. Tang XM, Patterson D, Hinds M (2001) Evaluating hydraulic fracturing in cased holes with cross-dipole acoustic technology. SPE Res Eval Eng 4(04):281–288. https://doi.org/10.2118/72500-PA
62. Tang XM, Patterson D (2009) Single-well S-wave imaging using multicomponent dipole acoustic-log data. Geophysics 74:211–223. https://doi.org/10.1190/1.3227150
63. Lee SQ, Tang XM, Su YD (2019) Shear wave imaging to determine near-borehole faults for ocean drilling exploration. Geophys J Int 217(1):288–293. https://doi.org/10.1093/gji/ggz023